PHYSICAL REVIEW D VOLUME 20, NUMBER 7 1 OCTOBER 1979

Baryon-baryon scattering in a one-boson-exchange-potential approach. III. A nucleon-nucleon and hyperon-nucleon analysis including contributions of a nonet of scalar mesons

M. M. Nagels, T. A. Rijken, and J. J. de Swart
Institute for Theoretical Physics, University of Nijmegen, Nijmegen, The Netherlands
(Received 24 October 1978)

The NN and YN results are presented from a one-boson-exchange-potential model. It consists of local potentials due to exchanges of members of the pseudoscalar, vector, and scalar-meson nonets. SU(3) relations are assumed for the axial-vector couplings of the pseudoscalar mesons, for the electric and magnetic couplings of the vector mesons, for the direct couplings of the scalar mesons, and for the hard-core radii. In the fit to NN the nonstrange-meson–nucleon couplings are determined. The simultaneous YN analysis determines the F/D ratios and the SU(3) parameters of the scalar-meson nonet. The description of the NN data is good (χ^2/data = 2.17), and also of the Λp, $\Sigma^+ p$, and $\Sigma^- p$ data up to the pion production threshold. Very close to the ΣN threshold we find a ΛN resonance, which is dominantly in the $^3D_1$ wave. The Λp cross section is maximal just below the $\Sigma^+ n$ threshold at $E = 2128.918$ MeV, in agreement with the experimental results of Λp final state interactions. The poles belonging to the Λp resonance are located on the second Riemann sheet at $E = 2131.77 \pm i\, 2.39$ MeV.

I. INTRODUCTION

The present model F completes our series of hard-core potential models, which can describe simultaneously all experimentally studied baryon-baryon (BB) systems. The formal aspects have been described extensively in the papers I and II.[1] Here we shall only spell out the differences in physical input compared to the previous models D (Ref 1) and E.[2] Model E differed from D in the fact that contributions of a nonet of scalar mesons were taken into account. The results were about the same as from model D. The main improvements over model D were a better value for $g_{NN\rho}$, a smaller value for α_P, and better values for the Λp scattering lengths. At the same time, however, some ambiguities were encountered in the SU(3) relations for the scalar-meson-nonet couplings, since the signs are not determined in the NN analysis. A further study of these ambiguities revealed the rather small sensitivity of the NN calculations to the values of the δ and ϵ' couplings. Varying these coupling constants, however, has large consequences for the YN analysis via the changes of the SU(3) parameters.

A less favorable point of models D and E was that the breaking of SU(3) was not only kinematical via the physical masses of the particles but also slightly dynamical via different hard cores in channels which belong to the same irreducible representation of SU(3), e.g., $^1S_0(pp)$ and $^1S_0(\Sigma^+p)$, which both belong to a $\underline{27}$.

The need for determining the scalar-octet couplings in YN without increasing the number of free parameters leads to a different hard-core prescription in this model: The hard cores are the same within the same irreducible representation. This leads to much stronger SU(3) constraints between the NN and YN analyses than previously. For example, the $^1S_0(pp)$ hard core will be the same as the $^1S_0(\Sigma^+p)$ hard core as well as for the $\underline{27}$ part of the $^1S_0(\Lambda N, \Sigma N; I=\frac{1}{2})$ states. In the following section we shall describe in detail how we handle the hard-core problem. It turns out that to describe the S waves in YN we are left with five parameters, just as many as in the previous models: α_P, α_V^m, $g_{\delta NN}$, $g_{\epsilon\Lambda\Lambda}$, $g_{\epsilon\Sigma\Sigma}$. The last three coupling constants together with $g_{\epsilon NN}$ fix then the SU(3) parameters of the scalar-meson nonet.

One of the advantages of the present hard-core treatment is that we can predict without any free parameter the $Y=0$ and $I=1,2$ BB states ($\Xi N, \Lambda\Sigma, \Sigma\Sigma$). The $Y=0$ and $I=0$ BB states ($\Lambda\Lambda, \Xi N, \Sigma\Sigma$) possibly require one S-wave free parameter. It is especially interesting to find out whether there are also $^3S_1$-$^3D_1$, $I=1$ resonances with $Y=0$, thus completing the $\underline{10^*}$ BB $^3S_1$-$^3D_1$ resonances and bound states, to which the deuteron and the ΛN resonances belong. This work is in progress.[3]

Next we discuss the differences in physical input for the various nonets compared to the previous models.

(i) The pseudoscalar nonet. The most important change is that we assume SU(3) relations for the axial-vector type of coupling, characterized by the interaction Hamiltonian density

$$\mathcal{H}_P = \frac{if_{13}}{m_\pi}\bar{\psi}_3\gamma_\mu\gamma_5\psi_1\partial^\mu\phi\,.$$

This choice has been made instead of the pseudoscalar coupling earlier used for several reasons,[4,5] one of them being that it can reconcile the large values for both $g_{\Lambda\Sigma\pi}$ and $g_{\Sigma\Sigma\pi}$ in the literature with SU(3).[5] Furthermore, we have changed the η-η' mixing angle to the value of the linear Gell-Mann–Okubo mass formula $\theta_P = -23°$. There are two reasons for this change. First, it allows a somewhat larger physical ηNN coupling, giving a better NN fit. Second, it is clear now that mesons and baryons are bound states of quarks and antiquarks. Therefore the argument of writing the mass operators as in the free-field Hamiltonians of elementary mesons or baryons becomes dubious. The baryons definitely favor linear mass relations. Mass formulas in models for the baryons and mesons have the same form for baryons and mesons, e.g., in the bag model.[6] Furthermore, a comparison of data in the backward hemispheres of the reactions $\pi^-p\to\phi n$ and $\pi^-p\to\omega n$, assuming the validity of the Okubo-Zweig-Iisuka rule,[7] leads to a value for the mixing angle which is close to the one from the linear mass formula.[8]

(ii) The vector-meson nonet. Here we assume as before SU(3) relations for the electric coupling at $t=0$ [for definiteness see Eq. (3.7) of II]

$$g^e_{13}=g_{13}\,,$$

with $\alpha^e_V=1$. The successes of SU(6) with respect to the magnetic moments of the baryons suggest that at $t=0$ the magnetic couplings

$$g^m_{13}=g_{13}+f_{13}$$

should obey SU(3) relations rather than the derivative coupling constants f_{13} as we have assumed before. Although we do not use the SU(6) prediction for α^m_V, we assume the magnetic couplings to satisfy SU(3) relations. α^m_V is determined in the fit to YN. For the ϕ-ω mixing angle we take $\theta_V=37.5°$ from the linear mass formula.

(iii) The scalar-meson nonet. The ϵ meson is treated the same as before. For the octet members we have used the $\delta'(1255)$,[9] $\epsilon'(1250)$, and $\kappa(1245)$. After the lengthy and time-consuming calculations had been completed, we would have rather preferred to use the $\delta(970)$ and $S^*(993)$, as these fit well together with the ϵ in a nonet of cryptoexotic $qq\bar{q}\bar{q}$ states.[10] The κ of this nonet is predicted to have a mass of 900 MeV. However, the calculations are rather insensitive to variations in the masses of the scalar-octet members. Merely the values of the physical ϵ couplings in the presence of ϵ_8-ϵ_1 mixing is the important effects. The main consequence of changing the masses of the octet members is a change of the singlet-octet mixing angle without changing significantly the physics (cf. Sec. III).

A final change consists in the values of the $\Lambda\Lambda\pi$, $\Lambda\Lambda\rho$, and $\Lambda\Lambda\delta$ coupling constants, which occur in the Λp and Λn charge-symmetry-breaking potentials. We have now from Λ-Σ^0 mixing[11] using the latest values of the baryon masses

$$f_{\Lambda\Lambda\pi}=-0.027f_{\Lambda\Sigma\pi}\,,\quad f_{\Lambda\Lambda\rho}=-0.027f_{\Lambda\Sigma\rho}\,,$$
$$g_{\Lambda\Lambda\delta}=-0.027g_{\Lambda\Sigma\rho}\,.$$

This way we have 11 parameters in the NN model: 4 hard cores and the 7 coupling constants f_π, $f_{\eta_1}, g_\rho, g_{\omega_1}, f_\rho, f_\omega, g_\epsilon$. The other coupling constants we encounter in NN ($f_{\eta_8}, f_\phi, g_\delta, g_{\epsilon'}$) are calculated via SU(3) relations with $F/(F+D)$ ratios from the YN fit or are fitted directly in YN.

In YN we have five parameters in the S waves ($\alpha_P, \alpha^m_V, g_{\delta NN}, g_{\epsilon\Lambda\Lambda}, g_{\epsilon\Sigma\Sigma}$), which are determined in a fit to the low-energy Λp, Σ^+p, and $\Sigma^-p\to\Sigma^-p$, $\Sigma^0 n$, Λn total cross sections. The parameters in the YN P waves (hard cores and a potential truncation parameter) are fixed by fitting to Σ^+p and $\Sigma^-p\to\Sigma^-p$, Λn angular distributions, and Λp total cross sections above the ΣN thresholds.

For NN we get a lower χ^2 than in models D and E, and better values for the coupling constants, the low-energy parameters, and the deuteron parameters. Owing to stronger constraints from SU(3) on the YN analysis we obtain a slightly worse fit than before, but still a very good one. There are improvements, especially in the values of α_p and the Λp scattering lengths. The singlet-octet mixing angle for the scalar-meson nonet comes out much larger than in models C (Ref. 12) and E (Ref. 3); it is almost ideal. However, the most interesting result is that we get ΛN-ΣN $^3S_1$-$^3D_1$ resonances around the ΣN thresholds. These are the $Y=1$ members of a $\underline{10}^*$, to which the deuteron belongs.

The plan of this paper is as follows. In Sec. II we discuss the SU(3) constraints for the hard cores. The results for the coupling constants emerging from the NN and YN fits form the topic of Sec. III. The NN results are presented and discussed in Sec. IV and the YN results in Sec. V.

II. THE HARD-CORE TREATMENT IN CONNECTION WITH SU(3)

The starting point is the assumption that SU(3) symmetry is only broken kinematically, i.e., via the physical masses of the mesons and baryons. This implies that all BB states in the same irreducible representation must have the same hard core. The breaking of SU(3) manifests itself then essentially in different ranges of the potentials and in the different reduced masses. When SU(3) symmetry would not be broken, we would calculate in the SU(3) eigenchannels. For the S waves the hard cores in the $\underline{27}$ and $\underline{10}^*$, as well as the complete interaction in these irreps, would be fixed in the NN fit. YN would have to supply the hard cores in the $\underline{8}_s$, $\underline{8}_a$, and $\underline{10}$. However, because of the breaking of SU(3) symmetry we are forced to use the isospin basis (and later on even the particle basis in order to account for breaking of isospin symmetry). In Table I we give the SU(3) content of the potentials in the isospin basis. When we encounter in some isospin state more SU(3) irreps requiring different hard cores as in $\Lambda N, \Sigma N(I=\frac{1}{2})$, we could choose the smaller core as the hard core and truncate the potential in the other irreducible representation at a larger value of r.

Because of SU(3) breaking we cannot simply project out V_{27}, etc., from $V_{\Lambda\Lambda}$, $V_{\Lambda\Sigma}$, and $V_{\Sigma\Sigma}(I=\frac{1}{2})$. Therefore we define the contributions from the various SU(3) irreps to the potentials in the isospin basis also in Table I, thereby keeping the kinematical breaking as much as possible.

A large reduction of the number of parameters is achieved by the observation that in a region where the potential is repulsive, the exact value of the hard core almost does not matter. So one can take as well in such a wave a convenient value: the hard core of one of the attractive components in the isospin or particle basis.

Next we discuss for the various waves how we handle the hard-core problem in practice.

(i) $^1S_0$. The potential in the $\underline{27}$ is attractive, and its hard core x_S is fixed in the NN fit. The same hard core applies to $\Sigma N(I=\frac{3}{2})$, which is also a pure $\underline{27}$ state. In ΛN and $\Sigma N(I=\frac{1}{2})$ we encounter next to a component in the $\underline{27}$ also a component in the $\underline{8}_s$ representation (Table I). The potential in the $\underline{8}_s$ turns out to be repulsive everywhere, and thus the value of its hard core is irrelevant. Therefore we can use the hard core x_s in all NN, ΛN, and ΣN channels for the $^1S_0$.

(ii) $^3S_1$-$^3D_1$. The potential in the $\underline{10}^*$ is attractive, and its hard core x_t is fixed in fitting the binding energy of the deuteron. The potential in the $\underline{10}$ is repulsive everywhere. So we may as well use x_t for $\Sigma N(I=\frac{3}{2})$, which is a pure $\underline{10}$ state (Table I). In the ΛN and $\Sigma N(I=\frac{1}{2})$ states we have next to an attractive potential in the $\underline{10}^*$ also an attractive potential in the $\underline{8}_a$ representation. So we have to determine in principle the hard core in the $\underline{8}_a$ state. However, it turns out that both S-wave hard cores x_S and x_T in the $\underline{27}$ and $\underline{10}^*$ are quite close to each other. We assume that the hard core in the $\underline{8}_a$ also does not differ much from x_S and x_T. It appears that the potential in the $\underline{8}_a$ is rather dependent on α_V^m. Therefore, if our assumption of all S-wave cores lying closely to each other is reasonable, we make only a small error in α_V^m when we take also for $\underline{8}_a$ the hard core x_T of the $\underline{10}^*$. On the other hand, a different choice of the hard core in the $\underline{8}_a$ implies the need of a truncation parameter for the potential belonging to the repre-

TABLE I. SU(3) content of the various potentials in the isospin basis and definition of the potentials in the SU(3) irreducible representations for broken SU(3).

Space-spin antisymmetric states $^1S_0, ^3P, ^1D_2, \ldots$		
$NN\to NN$	$I=1$	$V_{NN}\ (I=1)=V_{27}$
$\Lambda N\to \Lambda N$		$V_{\Lambda\Lambda}\ (I=\frac{1}{2})=(9V_{27}+V_{8s})/10$
$\Lambda N\to \Sigma N$	$I=\frac{1}{2}$	$V_{\Lambda\Sigma}\ (I=\frac{1}{2})=(-3V_{27}+3V_{8s})/10$
$\Sigma N\to \Sigma N$		$V_{\Sigma\Sigma}\ (I=\frac{1}{2})=(V_{27}+9V_{8s})/10$
$\Sigma N\to \Sigma N$	$I=\frac{3}{2}$	$V_{\Sigma\Sigma}\ (I=\frac{3}{2})=V_{27}$
$V_{27}^{\Lambda\Lambda}=V_{\Lambda\Lambda}-V_{\Lambda\Sigma}/3$	$V_{27}^{\Lambda\Sigma}=\frac{1}{2}\ (V_{27}^{\Lambda\Lambda}+V_{27}^{\Sigma\Sigma})$	$V_{27}^{\Sigma\Sigma}=V_{\Sigma\Sigma}\ (I=\frac{1}{2})-3V_{\Lambda\Sigma}$
$V_{8s}^{\Lambda\Lambda}=V_{\Lambda\Lambda}+3V_{\Lambda\Sigma}$	$V_{8s}^{\Lambda\Sigma}=\frac{1}{2}\ (V_{8s}^{\Lambda\Lambda}+V_{8s}^{\Sigma\Sigma})$	$V_{8s}^{\Sigma\Sigma}=V_{\Sigma\Sigma}\ (I=\frac{1}{2})+V_{\Lambda\Sigma}/3$
Space-spin symmetric states $^3S_1, ^1P_1, ^3D, \ldots$		
$NN\to NN$	$I=0$	$V_{NN}\ (I=0)=V_{10^*}$
$\Lambda N\to \Lambda N$		$V_{\Lambda\Lambda}\ (I=\frac{1}{2})=(V_{10^*}+V_{8a})/2$
$\Lambda N\to \Sigma N$	$I=\frac{1}{2}$	$V_{\Lambda\Sigma}\ (I=\frac{1}{2})=(V_{10^*}-V_{8a})/2$
$\Sigma N\to \Sigma N$		$V_{\Sigma\Sigma}\ (I=\frac{1}{2})=(V_{10^*}+V_{8a})/2$
$\Sigma N\to \Sigma N$	$I=\frac{3}{2}$	$V_{\Sigma\Sigma}\ (I=\frac{3}{2})=V_{10}$
$V_{10^*}^{\Lambda\Lambda}=V_{\Lambda\Lambda}+V_{\Lambda\Sigma}$	$V_{10^*}^{\Lambda\Sigma}=\frac{1}{2}\ (V_{10^*}^{\Lambda\Lambda}+V_{10^*}^{\Sigma\Sigma})$	$V_{10^*}^{\Sigma\Sigma}=V_{\Sigma\Sigma}\ (I=\frac{1}{2})+V_{\Lambda\Sigma}$
$V_{8a}^{\Lambda\Lambda}=V_{\Lambda\Lambda}-V_{\Lambda\Sigma}$	$V_{8a}^{\Lambda\Sigma}=\frac{1}{2}\ (V_{8a}^{\Lambda\Lambda}+V_{8a}^{\Sigma\Sigma})$	$V_{8a}^{\Sigma\Sigma}=V_{\Sigma\Sigma}\ (I=\frac{1}{2})-V_{\Lambda\Sigma}$

sentation with the larger core from the $\underline{10}^*$ and the $\underline{8}_a$. In fact many pairs of α_V^m and this truncation parameter are possible. Therefore we buy a possible error in the determination of α_V^m at the cost of not having to introduce a truncation parameter here. So we end up with one hard core x_T in all $^3S_1$-$^3D_1$ waves.

(iii) $^1P_1$. The potentials in both the $\underline{10}^*$ and $\underline{8}_a$ representations are strongly repulsive. Hence the results in these irreps are insensitive to hard-core variations. The potential in the $\underline{10}$, however, is strongly attractive. We can determine the hard-core radius of the $\underline{10}$ in a fit to the low-energy Σ^+p angular distribution, since the ^3P waves, being pure $\underline{27}$ states, are fixed via the hard core $x_{^3P27}$, determined in NN. The forward-backward asymmetry in the Σ^+p differential cross section is apart from the Coulomb contribution essentially determined by the $^1S_0$-$^1P_1$ interference. We use the hard core x_{1P} of the $\underline{10}$ also for the $\underline{10}^*$ and $\underline{8}_a$, because the small variations in the $^1P_1$ phase shifts in NN due to hard-core variations have almost no repercussion on the χ^2 in view of the poor status of this wave in the NN phase-shift analyses.

(iv) $^3P_{0,1,2}$. From the NN analysis we know the behavior of the potentials in the $\underline{27}$ states. The $^3P_0$ potential is very repulsive at short distances, the $^3P_1$ potential is everywhere repulsive, and the $^3P_2$ potential is attractive. So we can use the same hard core $x_{^3P27}$ in all three P waves of the $\underline{27}$, which is essentially fixed by the $^3P_2$ wave of NN. This is the hard-core prescription we use in NN, Σ^+p, and Σ^-n, which are pure $\underline{27}$ states.

The potentials in the $\underline{8}_s$, which appear in YN, $I=\frac{1}{2}$ states, are quite different. The $^3P_0$ potential in the $\underline{8}_s$ is strongly attractive, producing even bound states for the hard core $x \lesssim 0.46$ fm. Therefore the assumption of no bound states or resonances in the $^3P_0$ states puts a lower limit on the value of the hard core $x_{^3P8_s}$ in the $\underline{8}_s$. For larger values of x the $^3P_0(\Lambda N, \Sigma N)$ cross sections become very much independent of the hard-core radius, which is essentially due to the strong repulsion in the $\underline{27}$.

The $\underline{8}_s$ component of the $^3P_1$ potential is repulsive for $r \lesssim 0.54$ fm and attractive for $r > 0.54$ fm. It appears that the angular distribution of the reaction $\Sigma^-n \to \Lambda n$ at low energies is strongly dependent on the $^3P_1$-$^3D_1$ interference term. A forward-backward ratio >1 as in the experiment[3] can only be reached for values of $x_{^3P8_s} \gtrsim 0.50$ fm. So we can determine $x_{^3P8_s}$ in principle via fitting to the experimental $\Sigma^-p \to \Sigma^-p$, Λn angular distributions at $p_{\Sigma^-} = 160$ MeV/c.

The $^3P_2$ potential is attractive in the $\underline{8}_s$, and even quite stronger than in the $\underline{27}$. However, for $x_{^3P8_s} > x_{^3P27}$ no bound states or resonances appear.

We want to use the same hard-core radius $x_{^3P8_s}$ for all three $\underline{8}_s$ ^3P potentials, which are combinations of the $\underline{8}_s$ potentials V_c+V_σ, V_T, V_{SO}, V_Q. However, when using the isospin basis, we encounter for $I=\frac{1}{2}$ linear combinations of potentials in the $\underline{8}_s$ and $\underline{27}$ which have different hard cores. A similar problem arises using the particle basis, in which we actually perform the calculations. This problem is handled in practice in the following way: Since the $^3P_0$ and $^3P_1$ potentials in the $\underline{27}$ are strongly repulsive at short distances, it almost makes no difference when we use in these waves the larger hard core $x_{^3P8_s}$ also for the $\underline{27}$ potentials. In the $^3P_2$-$^3F_2$ states we use as hard core $x_{^3P27}$ and we truncate the potentials in the $\underline{8}_s$ at $x_{^3P8_s}$ by multiplying these potentials with the function

$$\xi(r) = 1 - \exp[-(r - x_{^3P27})^n/(x_{^3P8_s} - x_{^3P27})^n]\,,$$

where n is some high exponent (we have used $n=100$). When trying to determine the value of $x_{^3P8_s}$ in a χ^2 fit to the $\Sigma^-p \to \Sigma^-p$ and $\Sigma^-p \to \Lambda n$ differential cross sections, it appeared that for values of $x_{^3P8_s} \gtrsim 0.54$ fm the χ^2 is a very slowly decreasing function of $x_{^3P8_s}$. At the same time, however, the $\Lambda p \to \Lambda p$ and $\Lambda p \to \Sigma^0 p$ total cross sections above the ΣN thresholds decrease as a function of $x_{^3P8_s}$, thereby reducing the agreement with the experimental data. Therefore we have fitted $x_{^3P8_s}$ to a combined set of $\Sigma^-p \to \Sigma^-p$ and $\Sigma^-p \to \Lambda n$ differential cross sections, and of $\Lambda p \to \Lambda p$ and $\Lambda p \to \Sigma^0 p$ total cross sections above the ΣN thresholds.

For all $L \geq 2$ states we use the same hard-core radius $x_{L\geq 2}$, which is fitted in NN.

In Table II we summarize the hard-core prescription and the values of the hard cores, which have emerged from the fits. In Table II and also elsewhere in this paper we have given enough figures such that when using the given numbers our numerical results can be reproduced accurately.

III. COUPLING CONSTANTS

The NN coupling constants are given in Table III. The $g_{\pi NN}$ value has improved as compared to

TABLE II. Hard-core prescription in this model. Values are given in fm.

	NN, Σ^+p, Σ^-n	$\Lambda N, \Sigma N \to \Lambda N, \Sigma N$
$^1S_0$	$x_S = 0.52972$	x_S
$^3S_1$-$^3D_1$	$x_T = 0.52433$	x_T
$^1P_1$	$x_{1P} = 0.43014$	x_{1P}
$^3P_0$, $^3P_1$	$x_{^3P27} = 0.29278$	$x_{^3P8_s} = 0.52991$
$^3P_2$-$^3F_2$	$x_{^3P27}$	$x_{^3P27}$ [a]
$L \geq 2$	$x_{L\geq 2} = 0.68371$	$x_{L\geq 2}$

[a] The $\underline{8}_s$ components are multiplied with the cutoff function $\xi(r)$ defined in the text.

TABLE III. Nucleon-nucleon-meson coupling constants in this model. Figures between parentheses give information equivalent to those of neighboring columns. m denotes the mass.

	$g^2/4\pi$	$f^2/4\pi$	f/g	m (MeV)
π	(14.014)	7.752×10^{-2}		138.041
η	(7.596)	4.202×10^{-2}		548.8
η'	(8.835)	4.887×10^{-2}		957.5
ρ	0.627	27.343	(6.602)	770 $\Gamma=146$
ϕ	0.960	5.871	(−2.473)	1019.5
ω	12.462	5.339	(0.655)	783.9
δ	0.877			1255
ϵ'	0.252			1250
ϵ	25.580			760 $\Gamma=640$

TABLE IV. Parameters to be used in the SU(3) relations for the meson-baryon coupling constants: the octet coupling g_8, the singlet coupling g_1, the $F/F+D$ ratio α, and the singlet-octet mixing angle θ. The parameters are given for the axial-vector coupling of the pseudoscalar- (P) meson nonet, the electric (V^e) and magnetic (V^m) couplings of the vector-meson nonet, and the direct coupling of the scalar- (S) meson nonet.

	g_8	g_1	α	θ (deg)
P	0.278 43	0.283 59	0.409 11	−23
V^e	0.791 99	3.397 11	1	37.5
V^m	6.021 05	3.755 25	0.588 06	37.5
S	0.936 49	4.308 81	1.496 40	37.6964

paper I.[1] The $g_{\eta' NN}$ coupling is now considerably lower than in I (there called $g_{X^0 NN}$). This is mainly due to the change of the mixing angle. The value for $g_{\rho NN}$ is now excellent. This improvement over paper I can be viewed as an effect of the inclusion of the δ meson. Note that the $(f/g)_\omega$ value is larger than, for example, the estimate $(f/g)_\omega \leq 0.2$ of Höhler *et al.*[14] We shall not give an elaborate discussion of the NN coupling constants here and refer to paper I for more details on this matter.

In Table IV we give the SU(3) parameters g_1, g_8, α, and θ for the pseudoscalar-, vector-, and scalar-meson nonets. The parameters for the scalar-meson nonet have been calculated from the searched values for $g_{\epsilon NN}$, $g_{\epsilon\Sigma\Sigma}$, $g_{\epsilon\Lambda\Lambda}$, and g_δ. Furthermore, we used SU(3) for the axial-vector coupling of the pseudoscalar mesons. We get the nice result that α_p is almost the SU(6) value 0.4. For α_V^m we have a larger value than in the compilation of coupling constants.[5] In Sec. II we discussed that we allowed for a possible error in α_V^m in order to avoid the introduction of a new short-distance parameter in our model. For the scalar mesons we have determined $g_{\epsilon NN}$ in NN, $g_{\epsilon\Sigma\Sigma}$ in Σ^+p, and $g_{\epsilon\Lambda\Lambda}$ in ΛN. In terms of the SU(3) parameters g_1, g_8, θ_S, and α_S we have

$$g_{\epsilon NN}=\cos\theta_S\, g_1+\sin\theta_S\frac{1}{\sqrt{3}}(4\alpha_S-1)g_8\,,$$

$$g_{\epsilon\Lambda\Lambda}=\cos\theta_S\, g_1-\sin\theta_S\frac{2}{\sqrt{3}}(1-\alpha_S)g_8\,,$$

$$g_{\epsilon\Sigma\Sigma}=\cos\theta_S\, g_1+\sin\theta_S\frac{2}{\sqrt{3}}(1-\alpha_S)g_8\,.$$

From these relations we get

$$(g_{\epsilon\Lambda\Lambda}-g_{\epsilon NN})/(g_{\epsilon\Sigma\Sigma}-g_{\epsilon NN})=\frac{1}{3}\,\frac{2\alpha_S+1}{2\alpha_S-1}\,.$$

So α_S determines the correlation between $g_{\epsilon\Lambda\Lambda}$ and $g_{\epsilon\Sigma\Sigma}$. Therefore α_S is well determined by the YN data. Evidently this holds also for the product $\sin\theta_S g_8$. Because of the high mass of the ϵ' the results of the calculations are very insensitive to variations in ϵ' couplings. Therefore the product $\cos\theta_S g_8$ occurring in the ϵ' couplings is poorly determined. So the mixing angle can be determined only from the product $\sin\theta_S g_8$, when $g_8=g_\delta$ is given. Now g_8 depends on m_δ. We have taken here $m_\delta=1255$ MeV. Another choice might have been $m_\delta=970$ MeV; this would have led to a lower value for g_8 and so a larger value for θ_S.

IV. RESULTS FOR NN

The values of the 11 free parameters to be determined in the NN analysis are searched in a fit to the NN data, using the χ^2 second-derivative matrices of the Livermore phase-shift analysis[15] up to 330 MeV, the ${}^1S_0(pp)$ and ${}^3S_1(np)$ scattering lengths, and the deuteron parameters. The fit is very satisfactory, yielding $\chi^2/\text{data}=2.17$, compared to the 1128 data used in the Livermore analysis up to 330 MeV.

In Table V we have listed the resulting nuclear bar phase shifts. The scattering lengths and effective ranges of S and P waves [cf. Eqs. (30) and (32) of Ref. 1] are given in Table VI.

The hard-core radius x_T in the ${}^3S_1$-${}^3D_1$ waves has been fixed such that the experimental value for the binding energy of the deuteron is produced,

$$B=2.224\,64\text{ MeV}.$$

Table VI displays also the deuteron parameters: the D-state probability P_D, the electric quadrupole moment Q, the deuteron effective range $\rho(-B,-B)$, the asymptotic normalization $N_g{}^2$, and the S-D admixture A.

TABLE V. Nuclear bar pp and np phase shifts in degrees.

T_{lab} (MeV)	25	50	95	142	210	330
$^1S_0$	49.07	39.11	25.70	15.01	2.69	−14.19
$^3S_1$	79.23	60.66	41.64	28.58	14.90	−2.09
ϵ_1	2.02	2.58	3.38	4.35	6.05	9.77
$^3P_0$	9.04	12.33	10.72	5.95	−1.92	−15.10
$^3P_1$	−5.03	−8.49	−12.94	−16.69	−21.45	−28.80
$^1P_1$	−6.09	−8.74	−11.51	−14.01	−17.76	−24.55
$^3P_2$	2.32	5.57	10.43	13.74	16.39	18.15
ϵ_2	−0.82	−1.79	−2.86	−3.26	−3.08	−1.85
$^3D_1$	−2.94	−6.80	−12.51	−17.00	−21.65	−26.22
$^3D_2$	3.92	9.72	18.82	25.35	30.16	30.96
$^1D_2$	0.67	1.65	3.60	5.74	8.53	11.41
$^3D_3$	0.07	0.42	1.82	3.80	6.61	9.65
ϵ_3	0.57	1.68	3.51	4.95	6.33	7.51
$^3F_2$	0.10	0.34	0.77	1.13	1.40	1.01
$^3F_3$	−0.23	−0.70	−1.52	−2.21	−2.98	−4.03
$^1F_3$	−0.43	−1.16	−2.18	−2.85	−3.43	−4.16
$^3F_4$	0.02	0.11	0.41	0.88	1.75	3.41
ϵ_4	−0.05	−0.19	−0.52	−0.84	−1.25	−1.77
$^3G_3$	−0.05	−0.27	−0.92	−1.76	−3.06	−5.12
$^3G_4$	0.18	0.75	2.13	3.64	5.75	9.07
$^1G_4$	0.04	0.15	0.39	0.64	1.03	1.89
$^3G_5$	−0.01	−0.05	−0.16	−0.24	−0.25	−0.11
ϵ_5	0.04	0.21	0.70	1.25	1.99	3.09
$^3H_4$	0.01	0.03	0.10	0.20	0.37	0.64
$^3H_5$	−0.01	−0.08	−0.28	−0.52	−0.85	−1.33
$^1H_5$	−0.03	−0.17	−0.52	−0.87	−1.29	−1.78
$^3H_6$	0.00	0.01	0.04	0.09	0.21	0.51
ϵ_6	−0.00	−0.03	−0.11	−0.22	−0.38	−0.65

V. RESULTS FOR YN

The values for the five free parameters to be determined in the YN analysis are searched in a fit to a selected set of 35 best low-energy YN data [Table VII (data are from Refs. 13, 16–18)]. The obtained χ^2/data = 0.89 is quite satisfactory. In Table VII we compare our calculated values with the experimental ones.

Next we shall present the results for the two-particles channels in concise form. For single two-particles channels we give the nuclear bar phase shifts. The T-matrix amplitudes for the coupled two-particles channels are available on request.

A. Σ^+p, Σ^-n scattering

The Σ^+p "total" cross sections (for definition see Ref. 19) are compared with the experimental values in Table VII. It appears that most of the calculated values are larger than the experimental results, which is a consequence of the rather strong SU(3) constraints in the model. The same applies to the angular distribution at $p_{\Sigma^+} = 170$ MeV/c, where we obtain $\chi^2 = 5.3$ for seven data

TABLE VI. S- and P-wave effective-range parameters and deuteron parameters in units of fm.

	$^1S_0$	$^3S_1$	$^3P_0$	$^3P_1$	$^3P_2$	$^1P_1$
a	−7.827	5.459	−3.150	1.921	−0.267	2.764
r	2.710	1.806	3.393	−7.345	4.089	−6.406

P_D	Q	ρ $(-B,-B)$	N_g^2	A
6.36%	0.2840	1.810	0.7970	0.0261

TABLE VII. Comparison of the calculated and experimental values for the selected set of 35 best YN data (Ref. 19). The superscripts RH and M indicate the Rehovoth-Heidelberg (Ref. 16) and Maryland (Ref. 17) Λp data. The laboratory momenta are given in MeV/c and the total cross sections in mb.

$\Lambda p \to \Lambda p$ $\chi^2=3.5$			$\Lambda p \to \Lambda p$ $\chi^2=2.1$		
p_Λ	$\sigma_{\rm exp}^{\rm RH}$	$\sigma_{\rm th}$	p_Λ	$\sigma_{\rm exp}^{\rm M}$	$\sigma_{\rm th}$
145	180 ± 22	210.2	135	209 ± 58	230.1
185	130 ± 17	145.0	165	177 ± 38	174.9
210	118 ± 16	114.5	195	153 ± 27	132.0
230	101 ± 12	94.6	225	111 ± 18	99.2
250	83 ± 9	78.1	255	87 ± 13	74.4
290	57 ± 9	53.0	300	46 ± 11	48.1
$\Sigma^+p \to \Sigma^+p$ $\chi^2=2.8$			$\Sigma^-p \to \Sigma^-p$ $\chi^2=1.8$		
p_{Σ^+}	$\sigma_{\rm exp}$	$\sigma_{\rm th}$	p_{Σ^-}	$\sigma_{\rm exp}$	$\sigma_{\rm th}$
145	123 ± 62	119.9	142.5	152 ± 38	147.0
155	104 ± 30	112.0	147.5	146 ± 30	142.9
165	92 ± 18	105.1	152.5	142 ± 25	137.0
175	81 ± 12	98.8	157.5	164 ± 32	132.4
			162.5	138 ± 19	128.1
			167.5	113 ± 16	123.9
$\Sigma^-p \to \Sigma^0 n$ $\chi^2=6.2$			$\Sigma^-p \to \Lambda n$ $\chi^2=5.4$		
p_{Σ^-}	$\sigma_{\rm exp}$	$\sigma_{\rm th}$	p_{Σ^-}	$\sigma_{\rm exp}$	$\sigma_{\rm th}$
110	396 ± 91	178.2	110	174 ± 47	241.5
120	159 ± 43	158.1	120	178 ± 39	209.3
130	157 ± 34	142.1	130	140 ± 28	183.7
140	125 ± 25	129.0	140	164 ± 25	162.9
150	111 ± 19	118.2	150	147 ± 19	145.8
160	115 ± 16	109.3	160	124 ± 14	131.6
$r_R^{\rm exp}=0.468 \pm 0.010$			$r_R^{\rm th}=0.445$	$\chi^2=5.3$	

TABLE VIII. Σ^+p and Σ^-n S- and P-wave effective-range parameters in units of fm. The superscript C denotes the presence of the Coulomb interaction.

	$^1S_0$	$^3S_1$	$^3P_0$	$^3P_1$	$^3P_2$	$^1P_1$
a^C	−3.20	0.70	−2.80	1.84	−0.093	−1.96
r^C	3.87	−2.11	3.80	−7.09	36.2	3.62
a	−3.84	0.62	−2.29	1.49	−0.084	−1.65
r	4.03	−1.91	4.33	−8.67	81.4	3.70

points. The singlet Coulomb interference is almost opposite to the triplet contribution. The shape of the angular distribution is thus essentially determined, apart from the Coulomb forward peak, by the $^1S_0$-$^1P_1$ interference, which is large.

The scattering lengths and effective ranges in the S and P waves are given in Table VIII for the expansions Eqs. (30) and (32) of Ref. 1. The values for the $^1S_0$ and ^3P low-energy parameters are, as expected, of the same order as those of pp (cf. Table VI), both being in the same $\underline{27}$ representation of SU(3). In Table IX the nuclear bar phase shifts for Σ^+p are listed. The same qualitative behavior of the $^1S_0$, ^3P, $^1D_2$, ... phase shifts is encountered as in pp (cf. Table V). We notice that the $^1P_1$ phase shift grows up to 69.58° at about $p_{\Sigma^+}=730$ MeV/c. This wave is also mainly responsible for the second maximum in the Σ^+p nuclear total cross section around $p_{\Sigma^+}=470$ MeV/c (Fig. 1).

TABLE IX. Σ^+p nuclear bar phase shifts in degrees.

p_{Σ^+} (MeV/c) $T_{\rm lab}$ (MeV)	200 16.7	400 65.5	600 142.8	800 244.0	1000 364.5
$^1S_0$	33.85	22.96	7.07	−8.63	−23.27
$^3S_1$	−13.50	−28.14	−43.28	−57.76	−71.02
ϵ_1	−2.08	−5.49	−7.06	−7.15	−6.54
$^3P_0$	5.52	10.30	3.91	−7.30	−19.61
$^1P_1$	6.15	39.62	66.40	69.13	64.14
$^3P_1$	−3.42	−10.73	−18.46	−26.41	−34.21
$^3P_2$	0.52	2.46	3.18	1.97	−0.12
ϵ_2	−0.41	−2.06	−3.37	−3.73	−3.21
$^3D_1$	0.34	1.65	1.83	−0.53	−5.20
$^1D_2$	0.32	1.92	4.62	7.51	8.91
$^3D_2$	−0.50	−2.74	−5.47	−8.67	−12.58
$^3D_3$	0.04	0.63	1.61	1.77	0.27
ϵ_3	−0.07	−0.72	−1.61	−2.33	−2.76
$^3F_2$	0.04	0.44	0.98	1.06	0.14
$^1F_3$	0.06	0.54	1.39	2.77	4.70
$^3F_3$	−0.09	−0.91	−2.14	−3.41	−4.78
$^3F_4$	0.01	0.15	0.65	1.50	2.42
ϵ_4	−0.02	−0.27	−0.77	−1.31	−1.78
$^3G_3$	0.00	0.13	0.43	0.77	0.92
$^1G_4$	0.01	0.20	0.57	1.08	1.85
$^3G_4$	−0.02	−0.34	−0.98	−1.67	−2.30
$^3G_5$	0.00	0.04	0.21	0.56	1.13

B. ΛN scattering

The fit to the low-energy Λp data is of the same quality as the one of model D (Ref. 1) in spite of the much stronger theoretical constraints in this model (Table VII). However, three features are quite different from the previous model D: the S-waves low-energy parameters, the presence of the ${}^3D_1$ resonance, and the repulsive potentials in some of the P waves.

The low-energy parameters of the S waves are given in Table X. Contrary to the results of model D, in this model the requirement of $|a_S| > |a_T|$, needed because of the spin assignment of ${}^3_\Lambda H$, is well satisfied for the charge-symmetric ΛN potential.

The second more pronounced difference is the occurrence of the ${}^3D_1$ ΛN resonances in this model. We notice that the ${}^3D_1$ Λp nuclear bar phase shift goes through 90° below the $\Sigma^+ n$ threshold (Table XI). In order to find out where the pole corresponding to this resonance is located we have made an effective-range expansion at the $\Sigma^0 p$ threshold. Thereby we have suppressed the ${}^3D_1$ ΣN waves as explained extensively in Ref. 19. In Table XII we give the parameters for the effective-range expansion

$$p^{L+1/2}(\overline{K}^J)^{-1}p^{L+1/2} = -A^{-1} + \tfrac{1}{2}(p^2 - p_0^2)^{1/2}R(p^2 - p_0^2)^{1/2}.$$

Here $\overline{K}^J$ is the mutilated K^J matrix where the ${}^3D_1$ ΣN channels have been cut out, A^{-1} is the inverse-scattering-length matrix, R is the effective-range matrix, $p^{L+1/2}$ and $(p^2 - p_0^2)^{1/2}$ are diagonal matrices with elements $p_i^{L+1/2}$ and $(p_i^2 - p_{0i}^2)^{1/2}$, where p_{0i} denotes the momentum at the $\Sigma^0 p$ threshold energy. Using this effective-range expansion we search the pole corresponding to the resonances. For $Q = 1$ the poles are located on the second Riemann sheet (for the center-of-mass momenta we have $\mathrm{Im}\, p_\Lambda < 0$, $\mathrm{Im}\, p_{\Sigma^+} > 0$, and $\mathrm{Im}\, p_{\Sigma^0} > 0$) at the positions

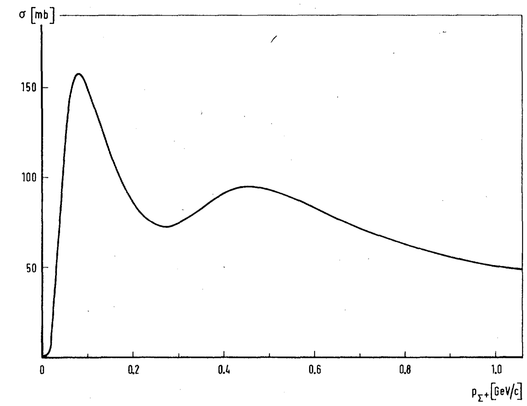

FIG. 1. $\Sigma^+ p$ total nuclear cross sections as predicted by the model.

$$E = 2131.77 \pm i2.39 \text{ MeV}.$$

We notice that $\mathrm{Re}E$ is 0.98 MeV larger than the $\Sigma^0 p$ threshold energy. For $Q = 0$ the situation is more complicated because of the presence of the Coulomb interaction in the $\Sigma^- p$ channel. When we switch off the Coulomb interaction it appears from the effective-range parameters (Table XII) that the poles are on the second Riemann sheet at the positions

$$E = 2137.27 \pm i2.56 \text{ MeV},$$

again about 1.6 MeV above the $\Sigma^- p$ threshold. An analysis with the Coulomb effective-range parameters (see, e.g., Ref. 19)

$$C(\eta)p^{L+1/2}(\overline{K}^J)^{-1}p^{L+1/2}C(\eta) + 2\eta p h(\eta) = -A^{-1} + \tfrac{1}{2}(p^2 - p_0^2)^{1/2}R(p^2 - p_0^2)^{1/2}$$

is also possible using the values of Table XII. However, we have not done this.

When we compare our pole values of the Λp resonance with determinations from Λp final-state interactions, we must keep in mind that all analyses parametrize the resonance as being a pure

TABLE X. Λp, ΛN, and Λn S- and P-wave effective-range parameters in units of fm.

	Λp		ΛN		Λn	
	a	r	a	r	a	r
${}^1S_0$	−2.18	3.19	−2.29	3.17	−2.40	3.15
${}^3S_1$	−1.93	3.35	−1.88	3.36	−1.84	3.37
${}^1P_1$	0.064	−28.0	0.047	18.6	0.029	230.0
${}^3P_0$	−0.065	32.1	−0.114	41.0	−0.164	34.6
${}^3P_1$	−0.015	1555.0	0.020	186.0	0.055	−69.8
${}^3P_2$	−0.189	8.75	−0.188	8.85	−0.187	8.37

TABLE XI. Λp nuclear bar phase shifts in degrees below the ΣN thresholds.

p_Λ (MeV/c)	100	200	300	400	500	600	633.4
$T_{\rm lab}$ (MeV)	4.5	17.8	39.6	69.5	106.9	151.1	167.3
$^1S_0$	22.93	28.97	26.02	19.74	12.38	4.95	2.88
$^3S_1$	20.75	26.95	24.69	19.13	12.49	5.65	0.50
ϵ_1	0.02	0.03	−0.16	−0.72	−1.82	−3.09	−1.48
$^3P_0$	0.04	0.24	0.24	−0.65	−2.82	−6.14	−7.39
$^1P_1$	−0.04	−0.33	−1.06	−2.42	−4.44	−7.00	−7.91
$^3P_1$	0.00	−0.05	−0.38	−1.12	−2.19	−2.90	−2.39
$^3P_2$	0.13	0.89	2.43	4.35	6.14	7.53	7.93
ϵ_2	0.00	−0.00	−0.05	−0.16	−0.28	−0.22	−0.07
$^3D_1$	0.00	0.07	0.53	2.22	7.39	30.03	93.83
$^1D_2$	0.00	0.04	0.28	0.89	1.95	3.35	3.85
$^3D_2$	0.00	0.07	0.38	1.10	2.28	3.76	4.29
$^3D_3$	0.00	0.04	0.24	0.75	1.60	2.68	3.06
ϵ_3	0.00	0.00	0.01	0.04	0.10	0.19	0.23
$^3F_2$	0.00	0.00	0.01	0.07	0.24	0.66	1.01
$^1F_3$	−0.00	−0.00	−0.00	0.00	0.01	0.03	0.03
$^3F_3$	0.00	0.00	0.02	0.05	0.10	0.18	0.22
$^3F_4$	0.00	0.00	0.01	0.07	0.20	0.44	0.55
$\sigma_{\rm tot}$ (mb)	310.3	125.9	48.2	18.2	8.4	17.5	51.2

$^3S_1$-wave resonance. From Breit-Wigner mass fits Tan[20] obtains two resonances at $M = 2128 \pm 0.2$ MeV, $\Gamma = 7.0 \pm 0.6$ MeV, and $M = 2138 \pm 0.7$ MeV, $\Gamma = 9.1 \pm 2.4$ MeV; Braun *et al.*[21] find in a high-statistics experiment $M = 2129.0 \pm 0.4$ MeV and $\Gamma = 5.9 \pm 1.6$ MeV. The cross section reaches its maximum in our calculations at $E = 2128.918$ MeV, which is 0.025 MeV below the $\Sigma^+ p$ threshold. This maximum agrees well with the maximum in the Λp invariant mass in the two experiments. However, the pole positions may differ, because these depend strongly on the parametrization used in the analyses.

The ΛN P-waves scattering lengths and effective ranges are given in Table X. Comparing these values and the P-wave phase shifts (Table XI) with the ones of the previous mosel D, we notice that the potentials are less attractive in the present model or even repulsive. The $^3P_0$ and $^3P_2$ phases show less attraction, whereas the $^1P_1$ and $^3P_1$ potentials are repulsive now. Calculations of the Λ well depth in nuclear matter with this potential give better results than with the one of model D, mainly owing to the changes in the P-waves contributions: about 34 MeV now, and about 40 MeV previously.[22]

TABLE XII. Inverse-scattering-length and effective-range matrices at the $\Sigma^0 p$ and $\Sigma^- p$ thresholds. The order of the states reads $\Lambda p(^3S_1)$, $\Lambda p(^3D_1)$, $\Sigma^+ n(^3S_1)$, $\Sigma^0 p(^3S_1)$, and $\Lambda n(^3S_1)$, $\Lambda n(^3D_1)$, $\Sigma^0 n(^3S_1)$, $\Sigma^- p(^3D_1)$, respectively. The dimensions of the matrix elements of A^{-1} are fm$^{-1-L-L'}$ and of R fm$^{1-L-L'}$. The subscript C denotes the presence of the Coulomb interaction in the $\Sigma^- p$ channel.

	A^{-1}			R		
	$\Lambda p \to \Sigma^0 p$	$\Lambda n \to \Sigma^- p$	$(\Lambda n \to \Sigma^- p)_C$	$\Lambda p \to \Sigma^0 p$	$\Lambda n \to \Sigma^- p$	$(\Lambda n \to \Sigma^- p)_C$
11	−15.08	−20.18	−19.93	65.03	111.23	107.93
12	10.88	14.98	14.68	−50.24	−83.51	−81.35
13	−1.69	−1.65	−1.67	10.12	11.69	11.75
14	1.25	2.57	2.58	−7.50	−17.66	−17.60
22	9.49	7.74	7.87	20.58	47.20	44.56
23	−1.64	−0.86	−0.89	−3.26	−5.49	−5.45
24	1.17	1.21	1.27	2.57	9.25	8.98
33	0.86	1.22	1.21	1.34	0.79	0.85
34	0.54	0.62	0.64	−1.82	−2.31	−2.35
44	1.25	0.78	0.92	0.18	2.81	2.84

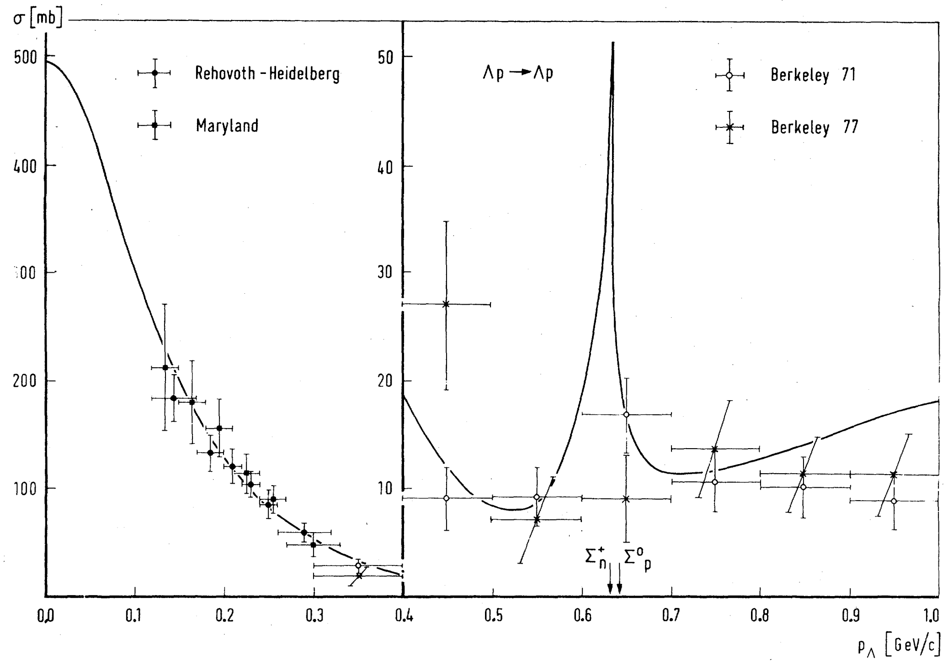

FIG. 2. Calculated Λp elastic total cross sections compared with the Rehovoth-Heidelberg (Ref. 16), Maryland (Ref. 17), and Berkeley (Refs. 23, 24) data.

The calculated angular distributions in the region 200–300 MeV/c have forward-backward ratios from 1.06 to 1.16 in agreement with experiment.[16]

The Λp elastic total cross sections up to $p_\Lambda = 1$ GeV/c are drawn and compared to experiment in Fig. 2. In the low-energy region ($p_\Lambda \leq 330$ MeV/c) the fit is very good with $\chi^2 = 3.5$ for the six Rehovoth-Heidelberg data and $\chi^2 = 2.1$ for the six Maryland data. In the momentum region above 0.3 GeV/c we see a reasonable agreement with the Berkeley data.[23,24] The calculated elastic total cross section in the region 0.6–0.7 GeV/c is at about 1.5 standard deviations higher than the experimental point of Berkeley 71 (Ref. 23) and about 3 standard deviations above the point of Berkeley 77 (Ref. 24). We have $\chi^2 \simeq 16$ for the seven Berkeley 71 data and $\chi^2 \simeq 19$ for the seven Berkeley 77 data.

The total cross sections for $\Lambda p \to \Lambda p, \Sigma^+ n, \Sigma^0 p$ above the ΣN thresholds are given in Table XIII. The calculated total cross sections for the reactions $\Lambda p \to \Sigma^+ n$, $\Sigma^0 p$ are a little higher than in the previous model D. However, the same remarks apply as before[1] as to the comparison (Fig. 3) of the $\Lambda p \to \Sigma^0 p$ data of the Berkeley groups.[23,24]

C. $\Sigma^- p$ scattering

1. $\Sigma^- p \to \Sigma^- p$

The fit to the total[19] cross sections of the Heidelberg group[17] is given in Table VII. The data are

TABLE XIII. $\Lambda p \to \Lambda p$, $\Sigma^+ n$, $\Sigma^0 p$ total cross sections in mb above the ΣN thresholds.

p_Λ (MeV/c)	$T_{\rm lab}$ (MeV)	$\Lambda p \to \Lambda p$	$\Lambda p \to \Sigma^+ n$	$\Lambda p \to \Sigma^0 p$
650	175.5	16.62	8.68	3.01
700	201.4	11.26	9.85	4.46
750	228.7	11.54	10.69	5.03
800	257.2	12.66	10.86	5.20
850	286.9	13.98	10.68	5.17
900	317.8	15.35	10.33	5.03
950	349.7	16.65	9.88	4.84
1000	382.6	17.86	9.40	4.62

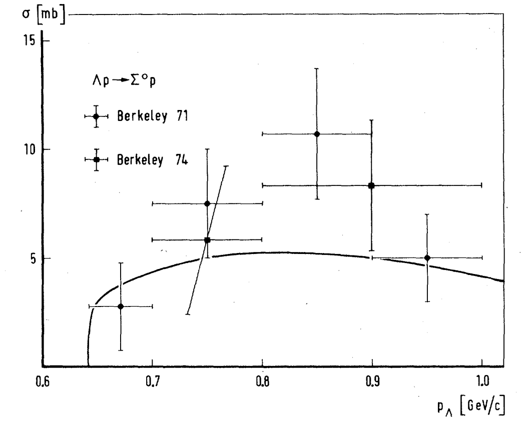

FIG. 3. Calculated $\Lambda p \rightarrow \Sigma^0 p$ total cross sections compared with the data of Refs. 23, 24.

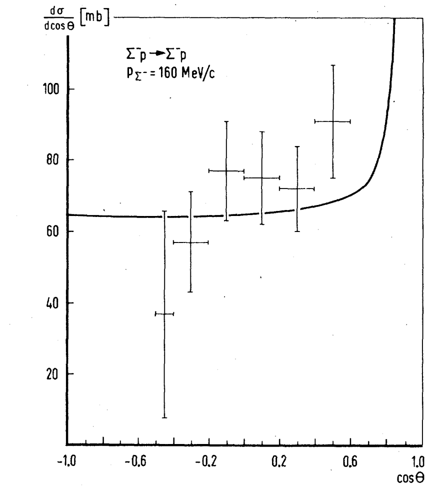

FIG. 4. Calculated $\Sigma^- p$ elastic differential cross section compared with the data (Ref. 18).

described well with $\chi^2 = 1.8$ for dix data points.

In Fig. 4 we compare the calculated angular distribution at $p_{\Sigma^-} = 160$ MeV/c with the results of the Heidelberg group.[18] Although the $\chi^2 = 4.8$ is reasonable for the six data points, the shape of the calculated differential cross sections seems too flat in the nonforward directions. The nuclear contributions to the differential cross sections, having a forward-backward ratio of 1.05, are flattened further by the destructive Coulomb interference terms.

In Table XIV we give the total nuclear cross sections for $\Sigma^- p$ elastic scattering up to $p_{\Sigma^-} = 600$ MeV/c. The scattering is strongly dominated by the ${}^3S_1 \rightarrow {}^3S_1$ amplitude for $p_{\Sigma^-} \lesssim 250$ MeV/c. At the higher energies the P-waves contributions are of comparable magnitude as the S waves and for $p_{\Sigma^-} \gtrsim 450$ MeV/c, these are a little larger. The contributions of the D waves are less than 5% in the whole energy region.

2. $\Sigma^- p \rightarrow \Sigma^0 n$

The calculated total cross sections are compared with the experimental values of the Heidelberg group[13] in Table VII. The agreement is excellent. From the total $\chi^2 = 6.2$ from the six data points 92% is due to the data point at $p_{\Sigma^-} = 110$ MeV/c. The calculated angular distribution at $p_{\Sigma^-} = 160$ MeV/c shows a forward-backward ratio of 1.67 mainly due to ${}^3S_1$-${}^3P_1$ and ${}^1S_0$-${}^1P_1$ interference. Unfortunately this angular distribution could not be measured.

In Table XIV we give the total cross sections for $\Sigma^- p \rightarrow \Sigma^0 n$ up to $p_{\Sigma^-} = 600$ MeV/c. The scattering is strongly dominated by the ${}^1S_0$ and ${}^3S_1$ waves for

TABLE XIV. $\Sigma^- p \rightarrow \Sigma^- p$, $\Sigma^0 n$, Λn total nuclear cross sections in mb.

p_{Σ^-} (MeV/c)	$T_{\rm lab}$ (MeV)	$\Sigma^- p \rightarrow \Sigma^- p$	$\Sigma^- p \rightarrow \Sigma^0 n$	$\Sigma^- p \rightarrow \Lambda n$
50	1.0	513.5	572.2	882.1
100	4.2	241.9	203.7	282.7
150	9.4	152.7	118.4	146.1
200	16.6	107.8	85.7	94.2
250	25.8	82.4	70.5	69.1
300	37.0	67.3	62.7	54.7
350	50.1	58.4	58.0	45.2
400	65.0	53.0	53.8	38.3
450	81.8	49.1	49.2	33.1
500	100.2	45.8	44.4	28.9
550	120.3	42.8	39.8	25.5
600	141.9	39.9	35.7	22.7

$p_{\Sigma^-} \leq 250$ MeV/c. At higher momenta the P-waves contributions are of comparable magnitude to those from the S waves and gradually these are larger. The contributions of the D waves to the total cross sections grow from about 4% at $p_{\Sigma^-} = 400$ MeV/c to about 10% at $p_{\Sigma^-} = 600$ MeV/c.

3. $\Sigma^- p \to \Lambda n$

In Table VII we compare the calculated total cross sections with the measured values of the Heidelberg group.[13] Although the $\chi^2 = 5.4$ for six data points is reasonable, our values seem a little higher than the experimental ones.

In Fig. 5 we compare the calculated angular distribution with the data of the Heidelberg group.[13] The calculated differential cross sections, yielding $\chi^2 = 12.6$ for 10 data points, seem too isotropic. This fact is also expressed by the forward-backward ratio $F/B = 1.12$ at $p_{\Sigma^-} = 160$ MeV/c compared to the measured value $F/B = 1.40 \pm 0.24$.[13] The isotropic shape of the angular distribution is mainly determined by the ${}^3S_1 \to {}^3D_1$ transition and the strong canceling of the large interference terms of the ${}^3S_1 \to {}^3D_1$ amplitude with the ${}^3P_1$ and the ${}^3P_2 \to {}^3F_2$ amplitudes. The value of the average polarization of the Λ at $p_{\Sigma^-} = 150$ MeV/c $\langle \vec{P} \cdot \hat{n} \rangle = -0.42$ agrees well with the Heidelberg result[13] $\langle \vec{P} \cdot \hat{n} \rangle = -0.6 \pm 0.4$ in the region 100–170 MeV/c.

In Table XIV we give the total cross sections for $\Sigma^- p \to \Lambda n$ up to $p_{\Sigma^-} = 600$ MeV/c. Below $p_{\Sigma^-} \gtrsim 200$ MeV/c the total cross section is for more than 75% due to the ${}^3S_1 \to {}^3D_1$ transition. For $p_{\Sigma^-} \gtrsim 350$ MeV/c this contribution constitutes about half of the total cross section. The other half is provided largely by the P waves.

In Table XV we present our predictions for the experimentally best accessible measurable quantities: the forward-backward ratio F/B and the polar-equatorial ratio P/E in the angular distribution, the left-right asymmetry $(L-R)/(L+R) = P_1^i \bar{\epsilon}$ in the case of incident Σ^- polarization P_1^i, the average polarization along the normal $\langle \vec{P} \cdot \hat{n} \rangle$, the average depolarization $\langle \mathfrak{D} \rangle$, the average asymmetry of the component of the final polarization in the direction perpendicular to the normal and the incident momentum $\langle \mathfrak{A}^{\perp} \rangle$, and the average asymmetry of the component of the final polarization along the incident momentum $\langle \mathfrak{A}^{\parallel} \rangle$, both with respect to the plane perpendicular to the initial polarization. Thereby we have included the amplitudes of the S and P waves and of the ${}^3S_1 \leftrightarrow {}^3D_1$ and ${}^3P_2 \to {}^3F_2$ transitions.

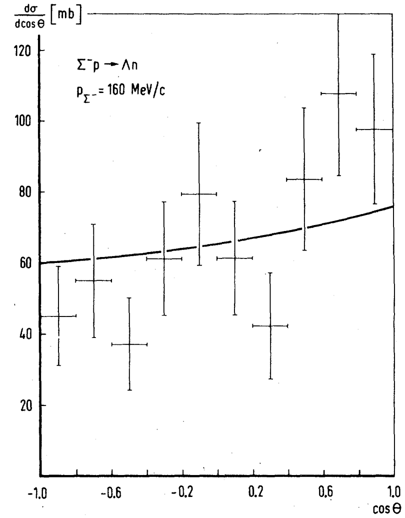

FIG. 5. Calculated differential cross section for the reaction $\Sigma^- p \to \Lambda n$ compared with the experimental angular distribution (Ref. 13).

Finally we mention that the value $r_R = 0.4450$ for the inelastic Σ^- capture ratio at rest is more than 2 standard deviations lower than the averaged experimental value (Table VII).

TABLE XV. Calculated measurable quantities for $\Sigma^- p \to \Lambda n$ at various laboratory momenta in MeV/c.

p_{Σ^-}	F/B	P/E	$\bar{\epsilon}$	$\langle \vec{P} \cdot \hat{n} \rangle$	$\langle \mathfrak{D} \rangle$	$\langle \mathfrak{A}^{\perp} \rangle$	$\langle \mathfrak{A}^{\parallel} \rangle$
50	1.04	1.00	0.07	−0.13	−0.28	0.29	0.02
100	1.08	1.01	0.16	−0.29	−0.28	0.26	−0.00
150	1.11	1.02	0.23	−0.42	−0.28	0.22	−0.06
200	1.12	1.04	0.28	−0.47	−0.27	0.16	−0.13
250	1.14	1.07	0.29	−0.46	−0.26	0.11	−0.19
300	1.16	1.12	0.28	−0.41	−0.25	0.04	−0.25
350	1.18	1.17	0.25	−0.35	−0.23	0.03	−0.26
400	1.18	1.23	0.21	−0.30	−0.22	0.00	−0.27
450	1.15	1.31	0.18	−0.25	−0.20	−0.01	−0.28
500	1.10	1.38	0.15	−0.21	−0.19	−0.02	−0.30
550	1.03	1.46	0.12	−0.18	−0.18	−0.02	−0.31
600	0.95	1.54	0.10	−0.16	−0.17	−0.02	−0.33

[1]M. M. Nagels, T. A. Rijken, and J. J. de Swart, Phys. Rev. D 12, 744 (1975); 15, 2547 (1977).

[2]M. M. Nagels, T. A. Rijken, and J. J. de Swart, in *Few Body Problems in Nuclear and Particle Physics*, edited by R. J. Slobodrian *et al.*, (Les Presses de l'Université de Laval, Québec, 1975); see also T. A. Rijken, Ph.D. thesis, University of Nijmegen, The Netherlands, 1975 (unpublished).

[3]W. M. Macek, M. M. Nagels, and J. J. de Swart (unpublished).

[4]J. J. de Swart and M. M. Nagles, Fortschr. Phys. 28, 215 (1978).

[5]M. M. Nagels, J. J. de Swart, H. Nielsen, G. C. Oades, J. L. Petersen, B. Tromborg, G. Gustafson, A. C. Iring, C. Jarlskog, W. Pfeil, H. Pilkuhn, F. Steiner, and L. Tauscher, Nucl. Phys. B109, 1 (1976).

[6]A. Th. M. Aerts, P. J. G. Mulders, and J. J. de Swart, Phys. Rev. D 17, 260 (1978).

[7]S. Okubo, Phys. Lett. 5, 165 (1963); G. Zweig, CERN Report No. 8419/TH142, 1964 (unpublished); J. Iizuka, K. Okada, and O. Shito, Prog. Theor. Phys. 35, 1061 (1966).

[8]D. Cohen *et al.*, Phys. Rev. Lett. 38, 269 (1977).

[9]N. M. Cason *et al.*, Phys. Rev. Lett. 36, 1485 (1976).

[10]R. L. Jaffe, Phys. Rev. D 15, 267 (1977).

[11]J. J. de Swart, M. M. Nagels, T. A. Rijken, and P. A. Verhoeven, Springer Tracts Mod. Phys. 60, 138 (1971).

[12]M. M. Nagels, T. A. Rijken, and J. J. de Swart, Phys. Rev. Lett. 31, 569 (1973).

[13]R. Engelmann, H. Filthuth, V. Hepp, and E. Kluge, Phys. Lett. 21, 587 (1966).

[14]G. Höhler *et al.*, Nucl. Phys. B114, 505 (1976).

[15]M. H. MacGregor, R. A. Arndt, and R. M. Wright, Phys. Rev. 182, 1714 (1969).

[16]G. Alexander, U. Karshon, A. Shapira, G. Yekutieli, R. Engelmann, H. Filthuth, and W. Lughofer, Phys. Rev. 173, 1452 (1968).

[17]B. Sechi-Zorn, B. Kehoe, J. Twitty, and R. A. Burnstein, Phys. Rev. 175, 1735 (1968).

[18]F. Eisele, H. Filthuth, W. Föhlisch, V. Hepp, E. Leitner, and G. Zech, Nucl. Phys. B37, 204 (1971).

[19]M. M. Nagels, T. A. Rijken, and J. J. de Swart, Ann. Phys. (N.Y.) 79, 338 (1973).

[20]T. H. Tan, Phys. Rev. Lett. 23, 395 (1969).

[21]O. Braun *et al.*, Nucl. Phys. B124, 45 (1977).

[22]J. Rožynek, private communication.

[23]J. A. Kadyk, G. Alexander, J. H. Chan, P. Gaposchkin, and G. H. Trilling, Nucl. Phys. B27, 13 (1971).

[24]J. M. Hauptman, J. A. Kadyk, and G. H. Trilling, Nucl. Phys. B125, 29 (1977).